Identification of Inclined Ionospheric Layers Using Analysis of GPS Occultation Data

Alexander G. Pavelyev, Kefei Zhang, Chuan-Sheng Wang, Yuriy Kuleshov, Yuei-An Liou, *Senior Member, IEEE*, and Jens Wickert

***Abstract*—The ionosphere and atmosphere may have significant impacts on the high-stable navigational signals of the Global Positioning System (GPS) in the communication link satellite to satellite. The classification of the different types of the ionospheric impact on the phase and amplitude of the GPS signals at altitudes of 40–90 km is introduced using the CHAllenging Minisatellite Payload (CHAMP) radio occultation (RO) data. An analytical model is elaborated for the description of the radio wave propagation in the stratified ionosphere and atmosphere. The propagation medium consists of sectors having the spherically symmetric distributions of refractivity. The newly developed model presents analytical expressions for the phase path and refractive attenuation of radio waves. The model explains significant amplitude and phase variations at altitudes of 40–90 km of the RO ray perigee associated with the influence of the inclined ionospheric layers. An innovative eikonal acceleration technique is described and applied to the identification and location of the inclined ionospheric layers using the comparative analysis of the amplitude and phase variations of the RO signals.**

***Index Terms*—Atmosphere, GPS, ionosphere gradient, LEO, radio occultation.**

I. Introduction

LIMB sounding radio occultation (RO) observations of the Earth's atmosphere and ionosphere have been recently carried out using Global Positioning System (GPS) radio signals at two frequencies $f_1 = 1575.42$ MHz and $f_2 = 1227.60$ MHz with a global coverage (e.g., [2], [7], [9], [10], [12], and [20]). When applied to the ionospheric investigations, the RO method can be compared with the global Earth- and space-based radio tomography (e.g., [3], [4], [6], [8], and [18]). The horizontal gradients in the ionosphere may introduce significant interference in the RO studies of the ionosphere and atmosphere. The mechanism of the ionospheric interference may be revealed by analyzing the radio wave propagation through locally spherical symmetric media.

Manuscript received April 27, 2010; revised August 31, 2010; accepted September 19, 2010. Date of publication January 16, 2011; date of current version May 20, 2011. This work was supported in part by the Australian Research Council under Grant ARC-LP0883288, by the International Science Linkage under Grant DIISR/ISL-CG130127, by the ASRP projects from the Department of Industry, Innovation, Science and Research, by the National Science Council and National Space Organization of Taiwan under Grants NSC 98-2111-M-008-012-MY3 and 98-NSPO(B)-IC-FA07-01(X), by the Russian Fund of Basic Research under Grant 10-02-01015-a, and by the program OFN-YI.15 of the Russian Academy of Sciences.

A. G. Pavelyev is with the Institute of Radio Engineering and Electronics of the Russian Academy of Sciences, 141120 Fryazino, Russia (e-mail: pvlv@ms.ire.rssi.ru).

K. Zhang, C.-S. Wang, and Y. Kuleshov are with the School of Mathematical & Geospatial Sciences, Royal Melbourne Institute of Technology University, Melbourne, Vic. 3001, Australia (e-mail: kefei.zhang@rmit.edu.au).

Y.-A. Liou is with the Center for Space and Remote Sensing Research, National Central University, Chung-Li 320, Taiwan (e-mail: yueian@csrsr.ncu.edu.tw).

J. Wickert is with the GeoForschungsZentrum Potsdam (GFZ-Potsdam), 14473 Potsdam, Germany (e-mail: wickert@gfz-potsdam.de).

Digital Object Identifier 10.1109/TGRS.2010.2091138

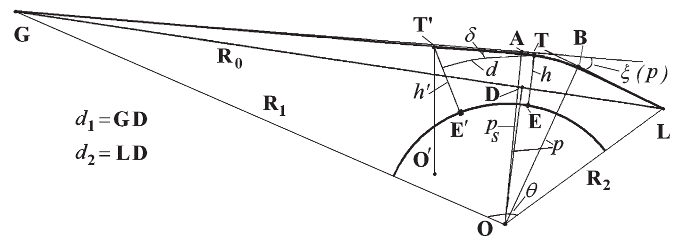

Fig. 1. Geometry of a radio ray path in the RO experiment.

During a RO event, the radio ray linking a LEO GPS receiver to a GPS satellite transmitter (marked by points L and G in Fig. 1, respectively) gradually immerses into the ionosphere and atmosphere. The LEO receiver measures the GPS phase delays and amplitudes of the RO signal for subsequent retrieval of the vertical profiles of the physical parameters of the ionosphere and atmosphere. Suppose that multipath propagation is absent, the RO inversion technique is based on two implicit assumptions: 1) the tangent point T, where the refractivity gradient is perpendicular to the RO ray direction, coincides with the RO ray perigee (Fig. 1), and 2) there is no other such point on the trajectory GTL. Under these assumptions, despite a prolonged path GTL, a relatively small area, with its center at point T, introduces the main contribution to the amplitude and phase variations of the RO signals [19]. In this case, the amplitude and phase variations of the RO signals are functions of the ray perigee height $h(T)$ (Fig. 1) and the satellites' positions and velocities. These functions can be used to determine the height dependence of the bending angle $\xi(p(h))$ if precise orbital data are given [12]. Abel transform is then applied to obtain the vertical profiles of the electron density in the ionosphere and the refractivity in the atmosphere as functions of the ray perigee height h [12]. From the amplitude, the vertical gradients of the electron density in the ionosphere and the refractivity in the atmosphere can be independently obtained [11], [19].

Usually, the ionospheric influence may be described as a relatively slow change in the phase path excess without noticeable variations in the amplitude of the RO signals. This change can be excluded by different methods of ionospheric correction [12], [17]. The strong amplitude and phase frequency dependent variation phenomenon in the RO signals are sometimes observed within the 40–90 km altitudes above the main part of the neutral atmosphere and below the E-layer of the ionosphere. This effect is analyzed in this paper.

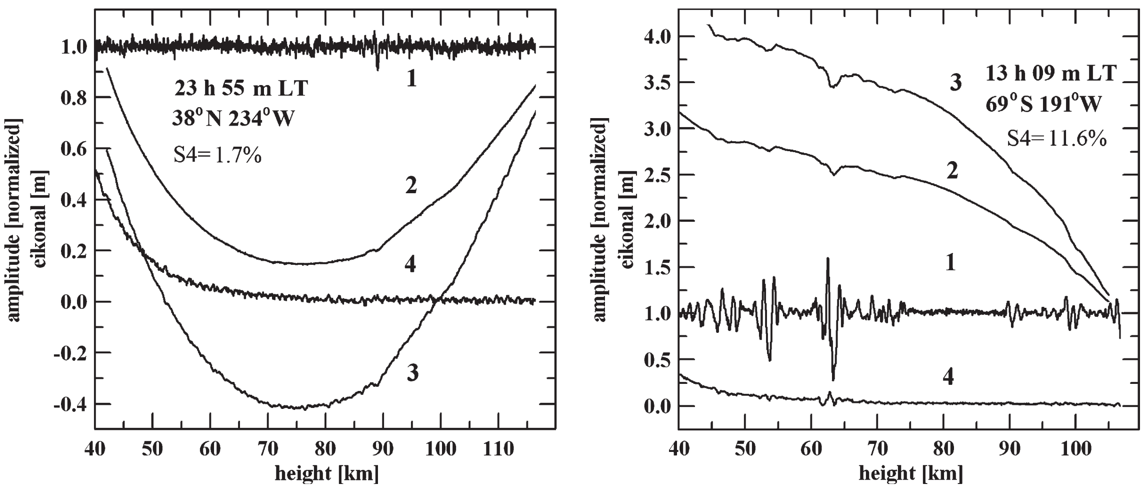

Fig. 2. Amplitude and phase measurements of the CHAMP RO signals in both (left) quiet and (right) slightly disturbed ionosphere (events No. 0174 and 0023; February 24 and June 16, 2003). The LT of the event and the coordinates of the atmospheric tangent point T are shown in the graphs. The S_4 index value is shown in the lower line of the insert.

The goals of this paper are the following: 1) to introduce different kinds of ionospheric impacts on the RO signals within the 40–90 km altitudes; 2) to present an analytical model for the refractive attenuation and phase path excess of the electromagnetic waves in locally spherical symmetric media; and 3) to demonstrate the possibility to identify contributions and to measure parameters of the inclined plasma layers by analyzing CHAMP experimental data. This paper is structured as follows. Section II introduces the different kinds of ionospheric impacts on the CHAMP RO signals. Section III presents an analytical model of wave propagation through the ionosphere and atmosphere of the Earth. Section IV gives an example of the ionospheric layer identification and the electron density retrieval. The conclusion is given in Section V.

II. Types of Ionospheric Influence on the CHAMP RO Signal

The RO experiment aboard CHAMP was activated on February 11, 2001 [19]. The carrier phase at frequencies f_1 and f_2 and the signal-to-noise ratio at f_1 are recorded at a sampling rate of 50 Hz. Previously, the RO technology has been based mainly on analyzing the phase of the electromagnetic wave after propagating through the ionosphere and atmosphere [7]. The amplitude of the RO signals presents new potential and capability for the research and observations of the atmosphere and ionosphere [10], [11], [16]. The high sensitivity of the amplitude variations to ionospheric plasma layers can be used to describe different kinds of ionospheric impacts on the RO signals. For the CHAMP RO experiments, quiet ionospheric conditions have come to light in the form of small values of the S_4 index of the amplitude scintillations averaged at the altitudes H in the 40–90 km interval

$$S_4 = \left[\left\langle (I(t) - \langle I\rangle)^2\right\rangle / \langle I\rangle^2\right]^{1/2} \tag{1}$$

where I is the intensity of the RO signals and $\langle I\rangle$ is the average intensity of the RO signals. An example of the quiet ionospheric conditions observed during the CHAMP RO experiments is shown in Fig. 2 (left panel). The amplitude curve 1 has low variations, with index $S_4 = 1.7\%$. The phase path excesses $\Phi_1(t)$ and $\Phi_2(t)$ at f_1 and f_2 are shown by curves 2 and 3, respectively. Curve 4 corresponds to the combined phase $\Phi(t)$ from the following ionospheric correction formula [12]:

$$\Phi(t) = \left[f_1^2\Phi_1(t) - f_2^2\Phi_2(t)\right] / \left(f_1^2 - f_2^2\right). \tag{2}$$

Examples of the significant variations of the phase and amplitude of the GPS RO signals are given in the following in the altitude intervals of the ray perigee 40–90 km. These examples support the suggestion that there exist inclined ionospheric layers located along the RO ray trajectory.

In Fig. 1, the apparent displacement of the height of the ionospheric layer Δh can be used in estimating its inclination δ with respect to the local horizontal direction [19]

$$\delta \approx (2\Delta h/a)^{1/2} \tag{3}$$

where a is the Earth's radius (Fig. 1). One can estimate, using Fig. 1, the horizontal distance d between the atmospheric and ionospheric tangent points if Δh is known.

The isolated quasi-regular event with the influence of the sporadic E-layer is shown in Fig. 2 (right panel). The fine structures corresponding to an inclined sporadic E-layer are seen in the height $h(T)$ intervals of 45–70 km. The phase and amplitude vertical distributions correspond to the inclined sporadic E-layers that are usually located at a height of about 93–103 km in the evening ionosphere. One can estimate the displacement of the ionospheric tangent point using (3). For $\Delta h = h' - h \approx 50$ km, one can obtain $\delta \approx 6^\circ$ and $d \approx (2\Delta h\ a)^{1/2} \approx 700$ km. These values may correspond to the sporadic E-layer at a height of 98 km, declined by 6° relative to the horizon and located at a distance of 700 km away from the atmospheric tangent point in the RO plane. An example of the event with high quasi-regular variations in the amplitude and phase of the CHAMP RO signal, with the magnitude of index $S_4 = 17\%$, is shown in Fig. 3(a). The eikonals at two

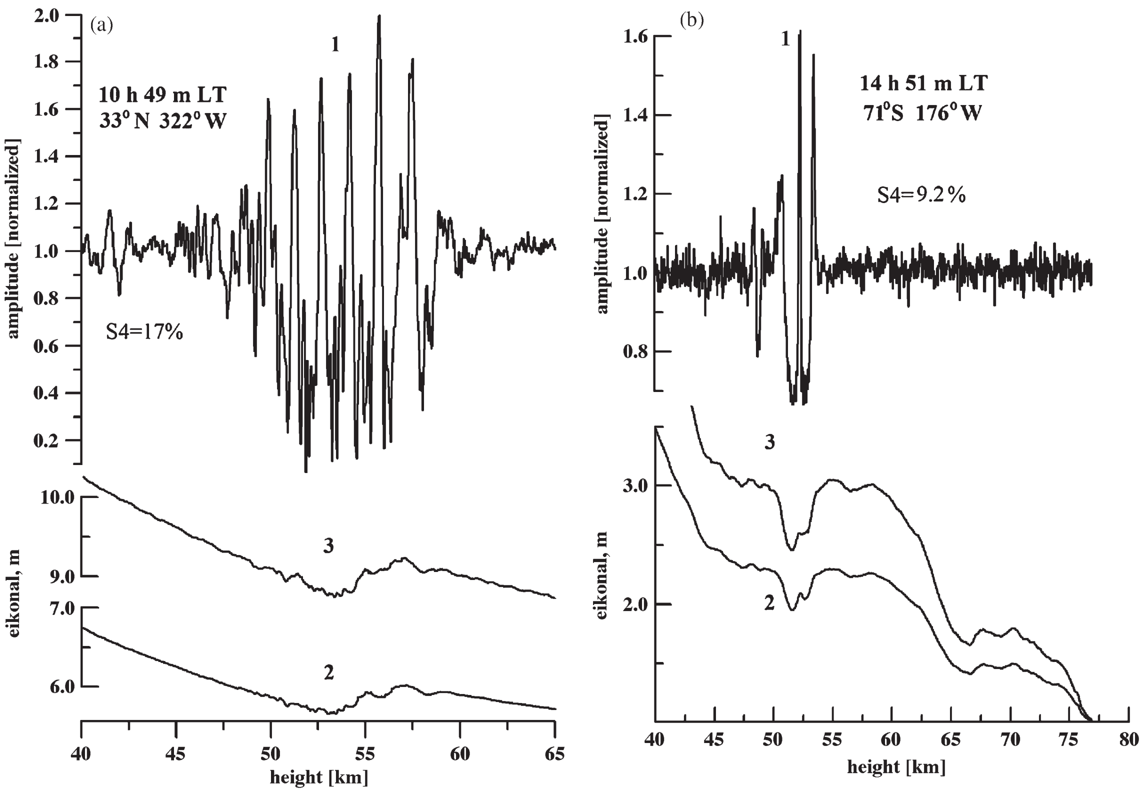

Fig. 3. (a) Quasi-regular variations in the amplitude and phase values of the CHAMP RO signals for event No. 0093 (February 24, 2003). (b) Amplitude and phase values of the CHAMP RO signals due to the diffraction of the electromagnetic waves in the ionosphere (event No. 0027; February 24, 2003). Curve 1 corresponds to the amplitude variations, and curves 2 and 3 are related to the eikonal variations at f_1 and f_2, respectively.

frequencies change in the interval $6 \leq \Phi_{1,2} \leq 10$ m. These variations may be associated with layers in the electron density distribution. A strong ionospheric influence with the diffraction structures in the RO signals is shown in Fig. 3(b) at the heights of 50–52.5 km. This case can be considered as a consequence of the diffraction of the electromagnetic waves on the sharp gradients of the electron density in an inclined sporadic E-layer. The examples of the noisy CHAMP events with significant amplitude variations $(S_4 = 10\%)$ are shown in Fig. 4. These events can be classified as typical cases, which are relevant to noisy ionospheric contributions caused by ionospheric irregularities in the equatorial region near midnight at 22 h 31 m and 23 h 21 m of the local time (LT) [Fig. 4 (left and right panels, respectively)]. The phase variations indicate sharp changes in the total electron content, which may correspond to bubbles moving in the disturbed region of the ionosphere.

Therefore, five types of ionospheric influence on the RO signals can be established at altitudes of 40–90 km. They are listed as follows

1) quiet events [type 1; Fig. 2 (left)];
2) isolated quasi-regular flashes in the amplitude and phase [type 2; Fig. 2 (right)];
3) regular events with quasi-periodical RO amplitude variations [type 3; Fig. 3(a)];
4) diffractive ionospheric events [type 4; Fig. 3(b)];
5) noisy events with highly incoherent ionospheric contributions to the amplitude of the RO signal (type 5; Fig. 4).

These types can be compared with the results of long-term (16 months) measurements of the signals propagating from a MARISAT satellite over the Indian Ocean at an elevation angle of 17.3° [5]. Both C- and S-types of the ionospheric amplitude scintillations of the radio signals are identified. The C-type is similar to noisy variations without any significant regular or periodical structure in the amplitude changes of the transionospheric signals. The S-type consists of quasi-regular structures which can be associated with the influence of the bubbles or other types of disturbances in the ionospheric plasma [5]. The CHAMP RO amplitude variations can also be recognized as the C- and S-types of the amplitude scintillations previously classified in the communication INMARSAT link at the same frequency band near 1.5 GHz [5]. The noisy C-type amplitude variations in the CHAMP RO signals at altitudes of 30–120 km are shown in Fig. 5 (left panel). Curves 1, 3, 4, and 5 describe the scintillations observed in the North and South Polar regions during the RO events of No. 0170, 0025, 0047, and 0196 (January 23, 2003). For events No. 0170, 0025, and 0196, the S_4 index was equal to 0.12, 0.13, and 0.21 (curves 1, 3, and 5, respectively), which corresponds to slightly disturbed ionospheric conditions. Event No. 0047 corresponds to the weakly disturbed ionosphere, with the S_4 index being equal to 0.053. Curves 2 and 6 (RO events No. 0019 and 0198; January 23, 2003) are relevant to the mid-latitudes with quiet (curve 2; $S_4 = 0.038$) and slightly disturbed (curve 6; $S_4 = 0.12$) ionosphere. The amplitude fluctuations during the RO event No. 0019 in the height interval of $h(T) = 30-110$ km (curve 2) were mainly caused by random receiver noise. The geographical

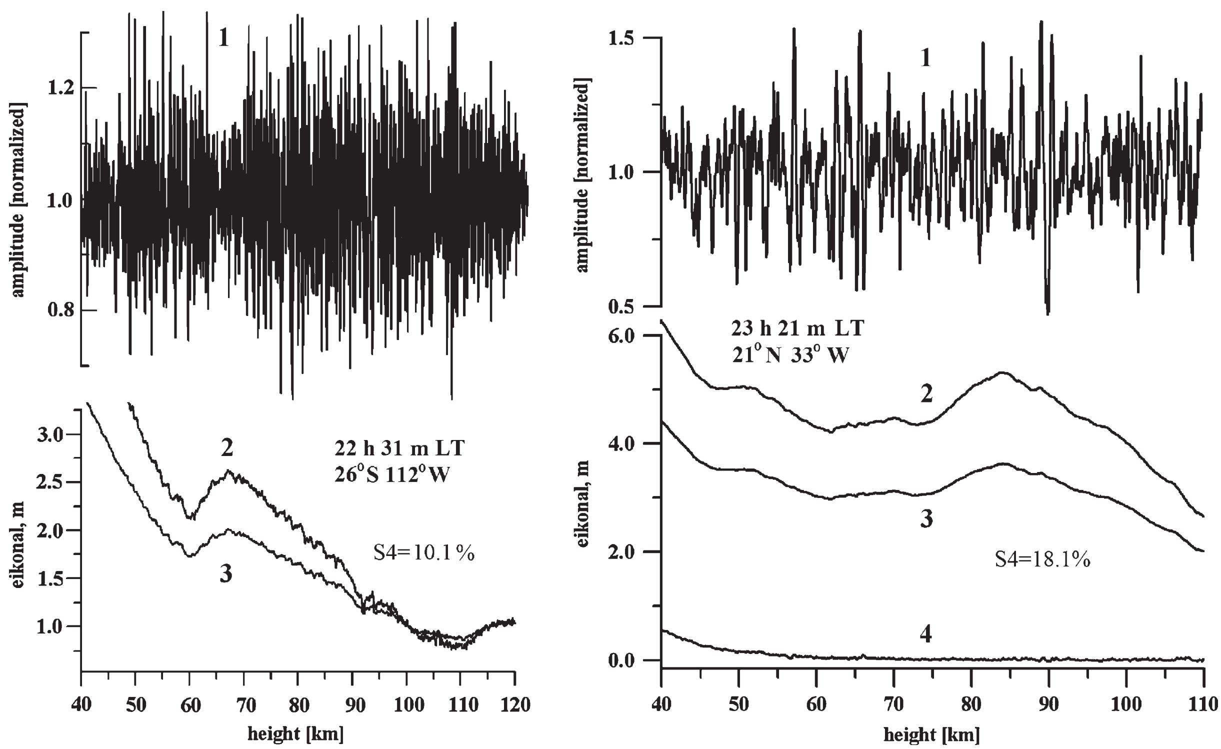

Fig. 4. Amplitude and phase values of the CHAMP RO signal for noisy events No. (left) 0069 and (right) 0014 (February 24, 2003) near the geomagnetic equator at local nighttime. Curve 4 (right panel) corresponds to the combined phase $\Phi(t)$ from formula (2).

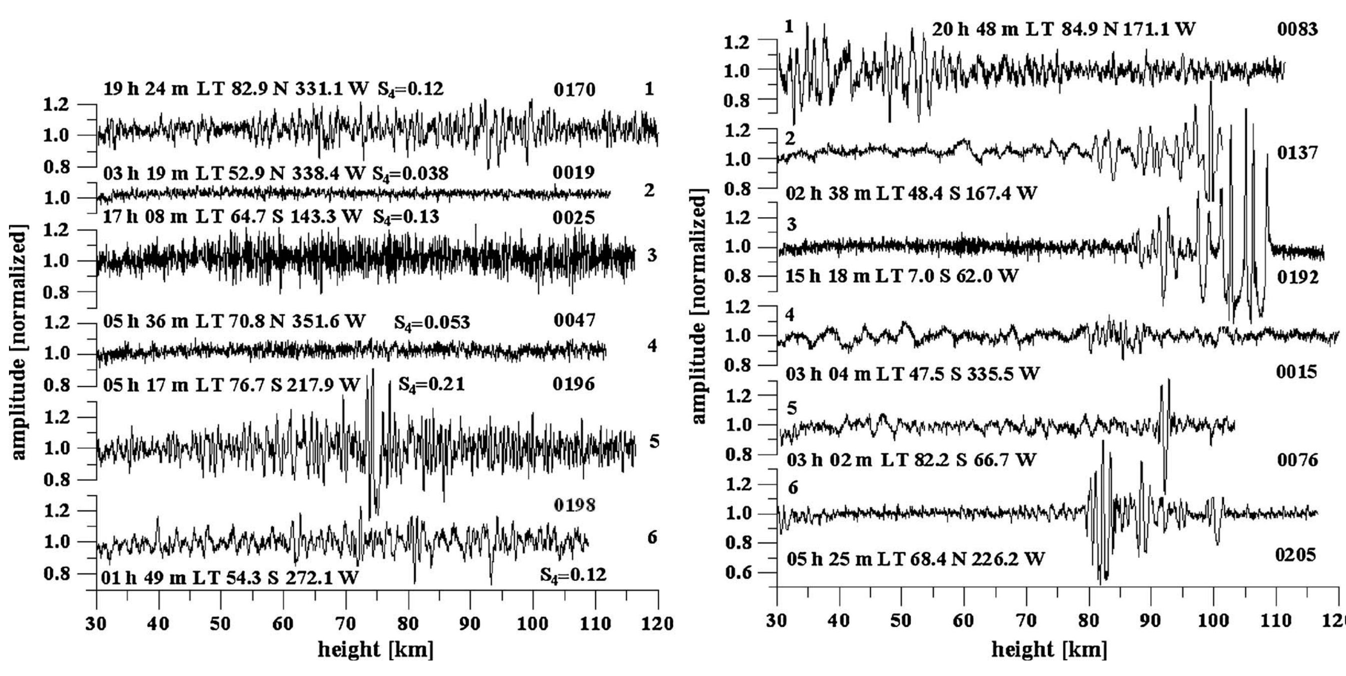

Fig. 5. (Left) C-type noisy and (right) S-type quasi-regular amplitude scintillations of the CHAMP RO signals. The legends indicate the LT, the geographical coordinates, the magnitude of the S_4 index, and the event's number of the RO experiments.

position and LT of the noisy RO events correspond to the same parameters of the noisy amplitude scintillations previously observed in transionospheric communications (e.g., [21]). The quasi-regular S-type amplitude variations are shown in Fig. 5 (right panel). Curves 2 and 4 correspond to the CHAMP RO events No. 0137 and 0015 (January 23; mid-latitude nighttime ionosphere), respectively; curves 1, 3, and 5 relate to events No. 0083, 0192, and 0076; and curve 6 corresponds to event No. 0205 on January 23, 2003 (equatorial daytime; south and north polar ionosphere). The inclined plasma layers in the E- or F-regions of the ionosphere might be the cause of the quasi-regular amplitude variations. Through comparisons of the data shown in Figs. 2–5, types 2, 3, and 4 of the RO amplitude variations can be recognized as the S-type amplitude

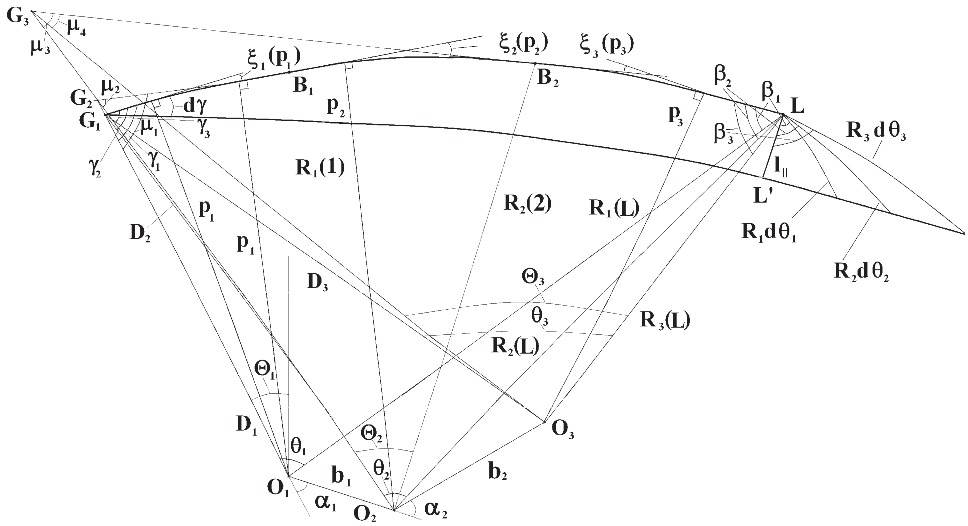

Fig. 6. Section of the ray tube by the RO plane containing transmitter G_1, receiver L, and centers of the local spherical symmetry O_1, O_2, and O_3. Lines G_1L and G_1L' are the top and bottom boundaries of the ray tube, respectively. Points B_1 and B_2 are the boundaries between two parts of the ionosphere G_1B_1 and B_2L and the atmosphere B_1B_2, and angles ξ_1, ξ_2, and ξ_3 are the bending angles corresponding to the three parts of the RO ray G_1B_1, B_1B_2, and B_2L.

scintillations observed in the transionospheric INMARSAT link by [5]. The noisy variations in the CHAMP RO signals correspond to the amplitude scintillations of the C-type. This coincidence in the types of CHAMP RO amplitude scintillations and the amplitude variations observed in the Earth-based experiments indicates the common ionospheric mechanisms of their origin.

III. Analytical Model for the Phase Path Excess and Refractive Attenuation of the RO Signal

A model of a medium composed of several spherical sectors was previously applied to estimate the effects of horizontal gradients in the atmosphere (e.g., [1]). A new analytical model describing the changes of the phase path and refractive attenuation of the electromagnetic waves propagated in the ionosphere and atmosphere is introduced in this paper. Three centers of local spherical symmetry associated with a single RO ray path in the ionosphere and atmosphere are located at different points O_1, O_2, and O_3 corresponding to three parts of the ray trajectory $G_1B_1B_2L$ in three spherical sectors having boundaries at points B_1 and B_2, respectively: G_1B_1 (the ionosphere between transmitter G_1 and the atmosphere), B_1B_2 (atmospheric part), and B_2L (the ionosphere between the receiver and the atmosphere; Fig. 6). Points G_1, L, O_1, O_2, and O_3 are assumed to belong to the plane $G_1B_1B_2L$. This assumption corresponds to the experimental RO data indicating a significant refraction effect in the plane of propagation. The central angles θ_1, θ_2, and θ_3 between directions to transmitter G_1 and receiver L have vertices located at points O_1, O_2, and O_3 (Fig. 6). The distances G_1O_1, G_1O_2, and G_1O_3 and LO_1, LO_2, and LO_3 are equal to D_1, D_2, and D_3 and $R_1(L)$, $R_2(L)$, and $R_3(L)$, respectively. Lines G_1L and G_1L' are, accordingly, the sections of the top and bottom boundaries of a ray tube by the RO plane. Points G_2 and G_3 (actually, G_2 and G_3 are apparent radio images of transmitter G_1 as seen from points B_1 and B_2) are the intersections of the tangents to the RO ray trajectory $G_1B_1B_2L$ at points B_1 and B_2 with the straight lines O_1G_1 and O_2G_2, respectively. The angles μ_1, μ_2, μ_3, and μ_4 have common vertices at points G_2 and G_3. Variables μ_1 and μ_2 are the angles between the tangent to the ray trajectory $G_1B_1B_2L$ at point B_1 and the directions of O_1G_2 and O_2G_2, respectively (Fig. 6). Variables μ_3 and μ_4 are the angles between the straight line G_3B_2 (the tangent to the ray trajectory $G_1B_1B_2L$ at point B_2) and the directions of O_2G_3 and O_3G_3, accordingly (Fig. 6). The dependence of the phase path excess and refractive attenuation on the impact parameter p may be separately considered for three parts of the RO ray trajectory $G_1B_1B_2L$. The phase path Φ corresponding to the ray $G_1B_1B_2L$ (Fig. 6) is a sum

$$\Phi = \sqrt{R_1^2 - p_1^2} + \sqrt{R_N^2 - p_N^2} + \sum_{i=1}^{i=N-1} b_i \cos(\gamma_i - \xi_i - \alpha_i) + \sum_{m=1}^{N} [p_m \xi_m(p_m) + \kappa_m(p_m)] \quad (4)$$

where N is the number of spherical sectors influencing the trajectory $G_1B_1B_2L$ ($N = 3$ for the geometry shown in Fig. 6); $R_i(l-1)$ and $R_i(l)$ are the distances from the ith spherical sector center O_i to the input and output of the lth spherical sector coinciding with boundaries B_{l-1} and B_l; for the case $N = 3$, B_0 and B_3 coincide with G_1 and L, respectively (B_1 and B_2 are shown in Fig. 6); $R_1(0) = D_1$; p_i, $\xi_i(p_i)$, and $\kappa_i(p_i)$ are the impact parameter, the bending angle, and the main refractivity part of the phase path corresponding to the ith spherical sector, respectively. The refractive index at boundaries B_{i-1} and B_i, with $i = 2, \ldots, N$, is assumed to be equal to one. The distances $R_i(l-1)$ and $R_i(l)$ may be determined using the impact parameters p_i, with $i = 1, \ldots, N$, if the angular coordinates of boundaries B_{i-1} and B_i, defined by the angles Θ_1, Θ_2, and Θ_3 (Fig. 6), are known.

An exact expression for the refractive attenuation X_L is derived in the Appendix. Using the refractive attenuation in N

spherical sectors with coplanar centers, one can obtain

$$X_L = R_0^2 \sin\gamma_1 \,/\, \{R_i \cos\beta_i |\partial\theta_i/\partial\gamma_1| d_{2N-2}(L) S(1)\cdots S(N)\}, \quad i = 1,\ldots,N$$
$$d_{2N-2}(L) = R_N(L)\sin[\Theta_N(L)]$$
$$S(i) = \sin\mu_{2i-1}/\sin\mu_{2i} \quad S(0) = 1 \tag{5}$$
$$\theta_i(L) = \pi + \xi(p_1) - \gamma_i - \beta_i, \qquad i = 1,\ldots,N \tag{6}$$
$$\xi(p_1) = \xi_1(p_1) + \cdots + \xi_N(p_N) \tag{7}$$
$$p_i = p_{i-1} + b_{i-1}\sin(\gamma_{i-1} - \xi_1 - \cdots - \xi_{i-1} - \alpha_{i-1}), \quad i = 2,\ldots,N. \tag{8}$$

The subscripts in (5)–(8) denote a number of spherical sectors, and the integer arguments correspond to a number of boundaries. $d_{2N-2}(L)$ is the length of the perpendicular from point L on the straight line linking the center of the Nth spherical sector (point O_N) with point G_N. The angles μ_{2k-1} and μ_{2k} have a common vertex at point G_k, and μ_{2k-1} and μ_{2k} are the angles between the ray tangent G_kB_{k-1} and the straight lines G_kO_{k-1} and O_kG_k, respectively. The relationship (5) for the refractive attenuation X_L is valid for any arbitrary number i from the interval $i = 1,\ldots,N$.

The developed analytical model allows ray tracing of the RO signals. If the impact parameter p_1 and the refractive angle in the first sector $\xi(p_1)$ are known, then one can consequently determine the impact parameters p_i, and the refractive angles $\xi(p_1)$ with $i = 2,\ldots,N$, from (7), (8), and then can recalculate the phase path $\Phi(p_1)$ and the refractive attenuation X_L from (5), (6) for an arbitrary N. Note the important feature of the introduced model. If, in the kth sector, the refraction effect is absent, then the dimension N of the model can be lowered to $N - 1$. In this case, the next equality fulfills

$$\mu_{2k-1} = \mu_{2k} \quad S(k) = 1. \tag{9}$$

In addition, (5) does not depend on the contribution from the kth spherical sector.

The phase path of the electromagnetic waves after propagating through the ionosphere and atmosphere may be considered according to relationship (4) as a quasi-linear function of the refractive angles. Therefore, the linear methods of the ionospheric correction introduced earlier [12], [17] should be effective in the case of propagation through several spherical symmetric sectors and undisturbed ionosphere. However, the amplitude of the RO signals is a nonlinear function of the refractive angle, and in the case of the disturbed ionosphere, it is a subject for strong perturbations.

The ionospheric contribution can be significant at different altitudes of the RO ray perigee in the 40–90 km interval if the following two necessary and sufficient conditions are fulfilled: 1) the ionospheric part of the RO signal path contains a tangent point, and 2) there is a refractivity layer with a sharp gradient that is perpendicular to the ray $G_1B_1B_2L$ in the vicinity of the tangent point. In the simplest case, when an inclined plasma layer exists only on one part of the ray $G_1B_1B_2L$ and the influence of the neutral atmosphere is weak, the analytical model predicts the displacement of the tangent point from the ray perigee T to a plasma layer. As a result, one may observe unusually strong amplitude and phase variations of the RO signals in the 40–90 km interval of the perigee height $h(T)$. It follows that the height of the inclined ionospheric layers does not coincide with the altitude of the RO ray perigee. If the location of the tangent point and the center of the local spherical symmetry are known, then it is possible to restore the vertical gradient of refractivity using the Abel transformation. This extends the applicable domain of the RO method.

IV. Identification of Plasma Layers

References [10], [11], and [15] detected and validated a connection between the phase excess $\Phi(p)$ (eikonal) acceleration and the refractive attenuation of the electromagnetic waves $X(t)$

$$1 - X(t) = ma = m\,dF_d/dt = m\,d^2\Phi(p)/dt^2$$
$$m = q/(dp_s/dt)^2 \quad q = (R_0 - d_2)d_2/R_0. \tag{10}$$

An inverse value m^{-1} may be considered as a module of the tangent point T centripetal acceleration oriented in the direction to point L. Formula (10) connects the refractive attenuation $X(t)$, the derivative of the Doppler frequency F_d on time, and the phase acceleration $a = dF_d(t)/dt = d^2\Phi(p)/dt^2$ via a relationship that is similar to the classical dynamics equation. The variations of the refractive attenuation $1 - X(t)$ may be considered as a ratio of the eikonal and centripetal accelerations of point T. The impact parameter p_s and the distances R_0 and d_2 are shown in Fig. 1. Parameters m and dp_s/dt may be evaluated from the orbital data. The distance d_2 can be evaluated from the relationship [15]

$$d_2 = 2R_0\beta\left[1 + 2\beta(1 - w/v) + (1 - 4\beta w/v)^{1/2}\right]^{-1},$$
$$\beta = mv^2/R_0 \quad m = [1 - X(t)]/a \tag{11}$$

where w and v are the velocity components of the GPS and LEO satellites, respectively, and they are perpendicular to the straight line GL on the plane GOL (Fig. 1). w and v are positive when they are oriented toward the point O direction and negative in the opposite case. Equation (10) presents a possibility to convert the phase acceleration a and/or Doppler frequency F_d to the refractive attenuation X_p [13], [15]. From these derived refractive attenuation and amplitude data, one can estimate the integral absorption of electromagnetic waves [15]. There is a possibility to apply the developed technique for the identification and location of the sharp layered sporadic Es structures in the ionosphere [13]. To consider the possibility to identify the plasma layer contribution in the RO signals, we will use a CHAMP RO event 0117 (January 14, 2001; 0 h 56 m LT; 76.4N, 172.7W) with strong quasi-regular amplitude and phase variations. The refractive attenuation of the CHAMP RO signals at the first GPS frequency f_1 (curve 1) and the phase path excesses at frequencies f_1 and f_2 (curves 2 and 3) as functions of the height of the RO ray perigee h are shown in Fig. 7 (left panel). Curves 2 and 3 have been obtained after subtracting a regular

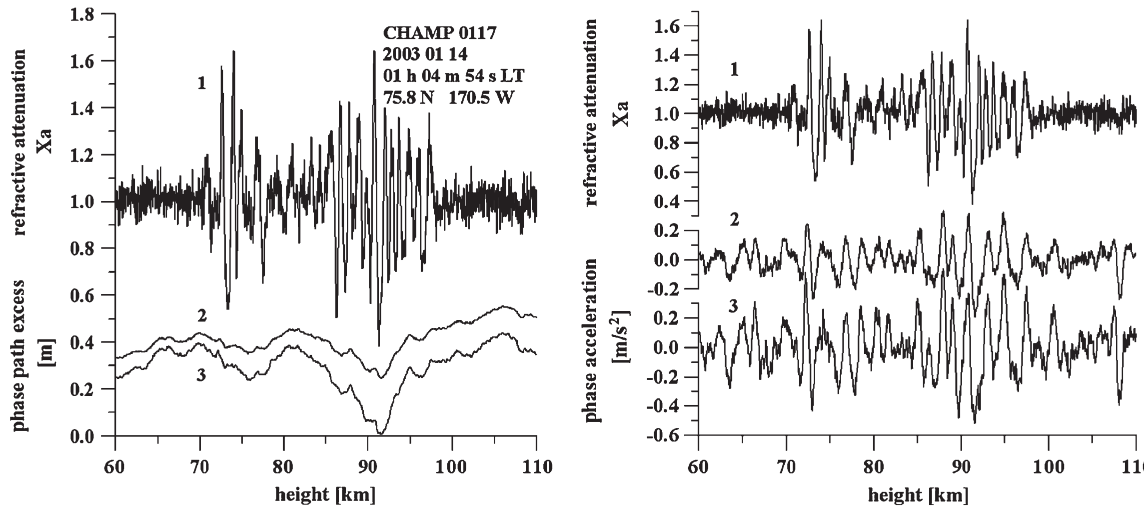

Fig. 7. Refractive attenuation at f_1 (curve 1) and the phase path excesses at f_1 and f_2 (curves 2 and 3; left). Comparison of the refractive attenuation at f_1 and the phase accelerations at f_1 and f_2 (curves 1, 2 and 3, right), respectively.

phase trend connected with the upper ionosphere influence. The form of the refractive attenuation variations indicates the impact of the ionospheric disturbances in the 72–98 km altitude. This disturbance consists of two patches which are responsible for the maxima in the intensity changes in the 72–78 and 84–96 km intervals of h. In the 78–84 km interval of height h, the intensity variations are notable. However, they are not so strong. The phase changes at frequencies f_1 and f_2 in Fig. 7 (left panel) also indicate a two-layered structure at altitudes of 75 and 90 km. The phase accelerations at both frequencies f_1 and f_2 [curves 2 and 3 in Fig. 7 (right panel)] reveal the fine structures in the phase of the RO signals. The phase acceleration a has been numerically estimated by double differentiation over a fixed time interval Δt. The value of Δt was equal to 0.42 s. The strongest variations of the phase acceleration are observed almost in the same altitude intervals as that for the refractive attenuation. In this interval, the phase acceleration and refractive attenuation variations are strongly connected, and they may be considered as coherent oscillations caused by layered structures. It is important that, at altitudes of below 72 km and higher than 98 km, the refractive attenuation variations are small and that they do not have any connection with the changes of the phase acceleration [Fig. 7 (right panel)]. This indicates a different incoherent mechanism of the significant phase variations at the heights of $h \leq 72$ km and $h \geq 98$ km. As a further identification step, a further examination is conducted to locate the indicated layers in the ionosphere. If parameter m is estimated from the experimental data using (10), it is possible to find the new value of distance $T'L \approx d_2'$ and to determine the displacement of the new tangent point T' and the location of a layer relative to point T (Fig. 1)

$$d = d_2' - \left(R_2^2 - p_s^2\right)^{1/2}. \tag{12}$$

The results of estimation of parameter m, displacement d, and corrected layer height h' are given in Table I as a function of the altitude h of the ray perigee T. The data presented in Table I correspond to the CHAMP GPS RO event No. 0117.

TABLE I
LOCATION OF THE IONOSPHERIC LAYERS

h	X_p-1	X_a-1	d, km	h', km	$\delta°$	m, s^2/m
97.61	0.06429	0.07053	140.74	99.163	1.26	0.87587
97.58	0.06584	0.07291	155.00	99.461	1.38	0.88391
97.55	0.06694	0.07458	164.73	99.673	1.47	0.88940
97.52	0.06633	0.07550	198.30	100.59	1.77	0.90861
97.49	0.06610	0.07563	206.26	100.81	1.84	0.91316
97.46	0.06481	0.07478	219.46	101.22	1.96	0.92078
97.42	0.06299	0.07309	228.50	101.50	2.04	0.92599
97.39	0.06081	0.07047	226.61	101.41	2.02	0.92484
97.36	0.05814	0.06694	216.38	101.02	1.93	0.91883
97.33	0.05460	0.06265	210.95	100.81	1.88	0.91563
72.23	0.04132	0.06316	714.35	112.09	6.39	1.17436
72.19	0.04029	0.05866	626.54	102.86	5.60	1.11844
72.16	0.03934	0.05328	498.98	91.618	4.46	1.04047
72.13	0.03786	0.04721	357.26	82.105	3.19	0.95806

The variations of the refractive attenuations $X_p - 1$ and $X_a - 1$ calculated from the amplitude and phase data and the estimated m values are shown in the second, third, and seventh columns in Table I as functions of the ray perigee height H in the following two intervals: 1) 97.33–97.61 km and 2) 72.13–72.23 km. These intervals correspond to a maximum in the absolute values of the refractive attenuation and phase acceleration variations that are relevant to curves 1 and 2, shown in Fig. 7 (right panel). The displacement d and the estimated value of the layer altitude h are presented in the forth and fifth columns in Table I, respectively. The displacement d changes between 140–210 and 357–714 km in the interval 1) and 2), respectively. These values correspond to the displacement of the tangent point from the ray perigee in the direction to point G. The corresponding corrections to the altitude h are about 2–6 and 20–30 km in the interval 1) and 2), respectively. This analysis suggests that the ionospheric layers are located in the entrance part of the ionosphere between point G and T (Fig. 1) at the distance d in the interval of 300–500 km. The corresponding values Δh change in the 2–30-km interval. The identification of the sporadic Es layer justifies the potential applications of the Abel transform in solving the inverse problem. The resulting

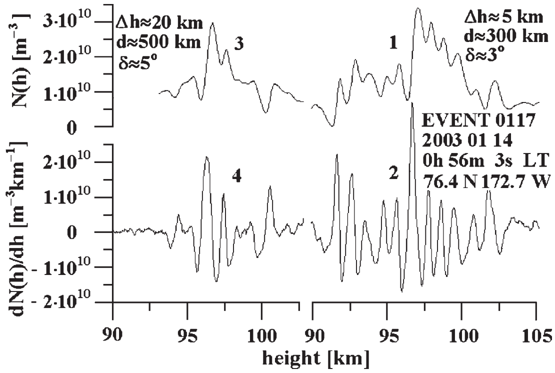

Fig. 8. Vertical distribution of the electron density and its gradient in the main parts of the two patches of the sporadic E-layer. Curves 1 and 3 describe the electron density distribution, and curves 2 and 4 are related to the vertical gradient of the electron density.

electron density distribution is shown in Fig. 8. As shown in Fig. 8, the electron density variations are concentrated in the interval $0 < N(h) < 3.5 \cdot 10^{10}$ [electrons/m^3]. These magnitudes of $N(h)$ are somewhat below the usual values of $N(h)$ for the sporadic E-layers. The height interval of the amplitude variations is nearly equal to the height interval of the variations in the electron density and its gradient. Two patches of the ionospheric layer are clearly shown in Fig. 8. The first patch of the layers is located on line GT at a distance of 300 km from point T (curves 1 and 2 in Fig. 8). It is concentrated in the 92–104-km interval, with an inclination to the horizontal direction δ of about 3°. The second patch (Fig. 8; curves 3 and 4) is located on the line GT in the 94–100-km interval at a distance of 500 km relative to the tangent point T (Fig. 1), with an inclination of about 5°.

The plasma density is small between two patches. The amplitude variations in the 70–96-km altitudes are associated with the sporadic E-layer located along the line GT in 92–104 km at a distance of 300–500 km relative to point T. The inclination of the sporadic E-layer changes along the line GT from 3° to 5°. Therefore, the introduced method appears to have a considerable potential to resolve the uncertainty in the location of the inclined layer between the parts GT and LT of the ray trajectory. Additional validation of this method through the analysis of the CHAMP data and the comparison with the ground-based ionosonde information is the task of our future work.

V. Conclusion

A new analytical model has been introduced to account for the local mechanism of the multiple-RO ionospheric effects, which incorporates the horizontal gradients in the ionosphere. The model gives analytical expressions for the phase path excess and the refractive attenuation of the electromagnetic waves propagating through the disturbed ionosphere. The new model can be used as a new analytical tool in calculating the parameters of the radio waves propagating through an inhomogeneous medium. The analytical presentation of the amplitude and phase variations of the radio waves gives some advantages compared with the phase screen method. The introduced analytical model suggests the potential for the applications of the Abel transform in estimating the electron density distribution in the inclined ionospheric plasma layers. The analysis of the CHAMP RO data and the analytical model have demonstrated the importance of the comparative analysis of the amplitude and phase channels of the satellite radio-holograms in classifying the ionospheric influence on the RO signals. The preliminary analysis reveals the following five types of ionospheric impacts on the CHAMP RO signals at the altitudes of the RO perigee 40–90 km: 1) quiet events; 2) isolated quasi-regular flashes (possible contribution of the inclined sporadic E-layers); 3) events with quasi-periodical changes of the amplitude and phase (the possible source is the wave structures in the electron density); 4) diffractive events with a clearly identifiable diffraction pattern in the amplitude and phase; and 5) events with noisy contribution of the ionospheric disturbances to the amplitude. The noisy and quasi-regular amplitude variations in the RO signals correspond to the earlier described C- and S-type amplitude scintillations in the transionospheric satellite-to-Earth links. The CHAMP RO data analysis has shown the possibility of the identification, location, and evaluation of the electron density distribution and its gradient in the inclined ionospheric layers. The tangent point displacement is the main cause of the systematic error in the RO estimation of the altitude of the inclined ionospheric layers. This conclusion may also be valid in the case of electromagnetic wave propagation in the satellite-to-Earth communication links.

Appendix
Derivation of the Refractive Attenuation

We choose a ray tube bounded by four surfaces. Two of them (G_1FLC and $G_1AL'D$) are perpendicular to the plane $G_1B_1B_2L$, and they intersect this plane along the rays G_1L and G_1L', respectively (Fig. 9). This ray tube has a nearly rectangular cross section $AFCD$ at point L, with the sizes $l_\parallel$ and $l_\perp$ in the plane surface $G_1B_1B_2L$ and in the perpendicular plane (Fig. 9). Owing to the local spherical symmetry, the tangents to the rays G_1F, G_1L, and G_1C at points B_1', B_1, and B_1'' intersect the straight line O_1G_1 at point G_2 located in the plane $G_1B_1B_2L$ (Fig. 9). Therefore, G_2 is a radio image of transmitter G_1 as seen from the boundary of the first and second sectors (point B_1). The plane $O_1G_1B_1B_2L$ is the bisection of the surfaces O_1G_1AF and O_1G_1CD. The surfaces $O_1G_1B_1'$ and $O_1G_1B_1''$ form the two plane side walls of the ray tube in the first spherical sector. The planes $O_1G_1B_1'$ and $O_1G_1B_1''$ intersect along the straight line G_1O_1, forming the dihedral angle $d\gamma$ (Fig. 9). The angle between the rays G_1L and G_1L' in the RO plane $G_1B_1B_2LL'$ at point G_1 is also assumed to be equal to $d\gamma$.

In the second spherical sector, these rays propagate according to the local spherical symmetry in the planes containing the center O_2 and the rays' tangents at points B_1' and B_1''. These planes are intersecting along the straight line O_2G_2, and they form the dihedral angle $d\gamma_1$. The distance $l_{\perp 1}$ at the boundary B_1 of the first spherical sector between the rays G_1B_1' and G_1B_1'' (Fig. 9) is

$$l_{\perp 1} = d_1 d\gamma, \qquad d_1 = S_1 \sin\mu_1 \tag{1A}$$

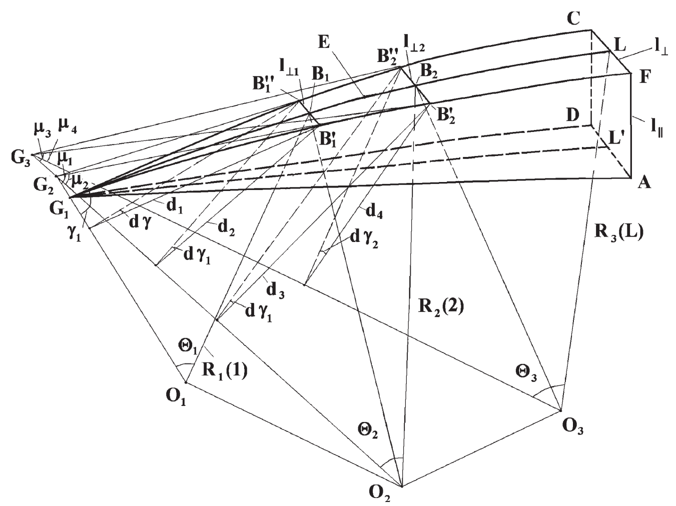

Fig. 9. Geometry of a ray tube of the electromagnetic waves propagating through three spherical symmetric sectors. Points G_1, B_1, B_2, and L are supposed to be located in the same plane with the centers of the spherical symmetry O_1, O_2, and O_3. Points G_2 and G_3 are the intersections of the tangents to the ray trajectory $G_1B_1B_2L$ at points B_1 and B_2 with the straight lines O_1G_1 and O_2G_2, respectively. The angles Θ_1, Θ_2, and Θ_3 have vertices at points O_1, O_2, and O_3. The values Θ_1, Θ_2, and Θ_3 determine the angles between directions O_1G_1, O_2G_2, O_3G_3 and O_1B_1, O_2B_2, O_3L, correspondingly. The exit ray tube cross section $AFCD$ at point L is nearly rectangular, and it has the sizes $l_{\|}$ and $l_{\perp}$ in the plane surface $G_1B_1B_2L$ and in the perpendicular plane, respectively.

where S_1 is the distance G_2B_1. At the boundary B_1 in the second spherical sector, the distance $l_{\perp 2}$ between the rays $B_1'B_2'$ and $B_1'B_2''$ is equal to

$$l_{\perp 2} = d\gamma_1 d_2, \qquad d_2 = S_1 \sin\mu_2 \tag{2A}$$

where d_1 and d_2 are the lengths of the perpendiculars from point B_1 on the straight lines O_1G_2 and O_2G_2, correspondingly. The size $l_\perp$ satisfies a continuity requirement at B_1

$$l_{\perp 1} = l_{\perp 2}. \tag{3A}$$

The next connection between the dihedral angles $d\gamma$ and $d\gamma_1$ follows from (1A)–(3A)

$$\begin{aligned} d\gamma_1 &= d\gamma\, d_1/d_2, \qquad d_1/d_2 = \sin\mu_1/\sin\mu_2 \\ d\gamma_1 &= d\gamma \sin\mu_1/\sin\mu_2. \end{aligned} \tag{4A}$$

From (2A) and (4A), the distance $l_{\perp 2}$ in the second sector can be expressed as

$$l_{\perp 2} = d\gamma_1 d_2(E) = d\gamma d_2(E) \sin\mu_1/\sin\mu_2 \tag{5A}$$

where $d_2(E)$ is the length of the perpendicular from the current point E on the ray G_1L on the straight line O_2G_2. The same procedure can be applied in finding the dihedral angle $d\gamma_2$ at the boundary B_2 between the second and the third sectors

$$\begin{aligned} d\gamma_2 &= d\gamma_1\, d_3/d_4, \qquad d_3/d_4 = \sin\mu_3/\sin\mu_4 \\ d\gamma_2 &= d\gamma_1 \sin\mu_3/\sin\mu_4 \\ &= d\gamma \sin\mu_1 \sin\mu_3/(\sin\mu_2 \sin\mu_4). \end{aligned} \tag{6A}$$

The length $l_{\perp 3}$ of the ray tube at point L can be found from the following equation:

$$l_{\perp 3} = d\gamma d_4(L) \sin\mu_1 \sin\mu_3/(\sin\mu_2 \sin\mu_4) \tag{7A}$$

where $d_4(L)$ is the length of the perpendicular from point L on the line O_3G_3 (Fig. 9). Owing to the local spherical symmetry, the tangents to the rays G_1F, G_1L, and G_1C at points B_2', B_2, and B_2'' intersect the straight line O_1G_1 in the point G_3 located in the plane $G_1B_1B_2L$ (Fig. 9). μ_3 and μ_4 are the angles with a common vertex at point G_3 between the tangent to the ray GF at point B_2' and directions O_2G_3 and O_3G_3, respectively (Fig. 9). From equations (2A)–(7A), the size $l_{\perp 3}$ then depends on the locations of the boundaries B_1 and B_2 and the centers of the spherical sectors O_1, O_2, and O_3.

The size $l_{\|}$ at point L may be found by considering the rays G_1L and GL' in the plane $G_1LO_1O_2O_3$, which is the vertical section of the ray tube (Figs. 6 and 9). The central angles θ_1, θ_2, and θ_3 between the directions to the transmitter G_1 and receiver L have vertices in the centers O_1, O_2, and O_3 of the spherical sectors (Fig. 6). The impact parameters in the corresponding spherical sectors are designated by p_1, p_2, and p_3 (Fig. 6). Owing to the condition of spherical symmetry, the impact parameters p_1, p_2, and p_3 satisfy the following relationships, which are valid inside the ith spherical sector:

$$p_i = n(R_i)R_i \sin\gamma_e, \qquad i = 1, 2, 3 \tag{8A}$$

where $n(R_i)$ is the refractive index and γ_e is the angle between the tangent to the ray trajectory G_1L at the current point E and direction to the center of the ith spherical sector. The tangents to the ray trajectory G_1L and the directions to the centers O_1, O_2, and O_3 make the angles γ_1, γ_2, and γ_3 at point G_1 and β_1, β_2, and β_3 at point L, respectively (Fig. 6). A method suggested in [14] is used to obtain an expression for $l_{\|}$. Three equivalent expressions are derived by considering the rectangular triangles having the common cathetus $LL'(l_{\|})$ and the differentials $R_i d\theta_i$ as the hypotenuses (Fig. 6)

$$l_{\|} = R_i(L) cos\beta_i \partial\theta_i/\partial\gamma_1 d\gamma, \qquad i = 1, 2, 3 \tag{9A}$$

where $R_i(L)$ is the distance O_iL (Fig. 6). Note that the partial derivatives of the central angles θ_i that are relative to the input angle γ_1 are evaluated with the distances $R_1(L), R_2(L), R_3(L)$ and $D_1(G_1), D_2(G_1), D_3(G_1)$ held constant. The relationship (9A) is valid for an arbitrary number i, with $i = 1, 2, 3$. The power W emitted by an isotropic antenna in the ray tube is equal to

$$W = Pd\Omega/4\pi = P\, sin\gamma_1 (d\gamma)^2/4\pi \tag{10A}$$

where P is the power of the transmitter and $d\Omega$ is the solid angle that is relevant to the ray tube.

The power flow in free space W_{L0} is equal to

$$W_{L0} = P/4\pi R_0^2. \tag{11A}$$

The refractive attenuation at point L X_L can be obtained as a ratio of the power flow in the ray tube $W_L = W/(l_\perp \cdot l_{\|})$ to the power flow in free space W_{L0} (11A)

$$\begin{aligned} X_L &= W_L/W_{L0} \\ &= R_0^2 \sin\gamma_1 / \left[d_4(L) R_i(L) cos\beta_i |\partial\theta_i/\partial\gamma_1| \sin\mu_1 \sin\mu_3 \right. \\ &\qquad \left. /(\sin\mu_2 \sin\mu_4) \right], \\ &\qquad i = 1,2,3 \quad d_4(L) = R_3(L) \sin\left[\Theta_3(L)\right] \end{aligned} \tag{12A}$$

where $\Theta_3(L)$ is the angle with the vertex at point O_3 between directions O_3G_3 and O_3L (Fig. 9). The relationships between the impact parameters (p_1, p_2, and p_3), central angles (θ_1, θ_2, and θ_3), and bending angles (ξ_1, ξ_2, and ξ_3) can be obtained using the geometry of the path $G_1B_1B_2L$ (Fig. 6)

$$\begin{aligned} p_2 &= p_1 + b_1 \sin(\gamma_1 - \xi_1 - \alpha_1) \\ p_3 &= p_2 + b_2 \sin(\gamma_2 - \xi_1 - \xi_2 - \alpha_2) \end{aligned} \tag{13A}$$

$$\begin{aligned} \theta_i &= \pi + \xi(p_1) - \gamma_i - \beta_i \\ \xi(p_1) &= \xi_1(p_1) + \xi_2(p_2) + \xi_3(p_3), \qquad i = 1,2,3. \end{aligned} \tag{14A}$$

Relationships (4) and (12A)–(14A) present the main content of the analytical model in the partial case of three spherical sectors. In plane $G_1B_1B_2L$, the phase path and the refractive attenuation depend on the sum of the phase changes and the bending angles in the spherical sectors, respectively, and they practically do not depend on the location of their boundaries. The effects of a spherical symmetric layer do not significantly depend on its location in the first, second, or third spherical sectors.

The introduced model may be generalized for an arbitrary number N (i.e., the number of spherical symmetric sectors with the centers of the spherical symmetry located in the same plane).

ACKNOWLEDGMENT

The authors would like to thank GFZ-Potsdam for giving access to the CHAMP RO data.

REFERENCES

[1] B. Ahmad and G. L. Tyler, "Systematic errors in atmospheric profiles obtained from Abelian inversion of radio occultation data: Effects of large-scale horizontal gradients," *J. Geophys. Res.*, vol. 104, no. D4, pp. 3971–3992, 1999.

[2] G. A. Hajj and L. J. Romans, "Ionospheric electron density profiles obtained with the Global Positioning System: Results from GPS/MET experiment," *Radio Sci.*, vol. 33, no. 1, pp. 175–190, 1998.

[3] D. Wen, Y. Yuan, J. Ou, and K. Zhang, "Ionospheric response to the geomagnetic storm on August 21, 2003 over China using GNSS-based tomographic technique," *IEEE Trans. Geosci. Remote Sens*, vol. 48, no. 8, pp. 3212–3217, Aug. 2010.

[4] N. Jakowski, R. Leitinger, and M. Angling, "Radio occultation techniques for probing the ionosphere," *Ann. Geophys., Suppl. V*, vol. 47, no. 2/3, pp. 1049–1066, 2004.

[5] Y. Karasawa, K. Yasukawa, and M. Yamada, "Ionospheric scintillation measurement at 1.5 GHz in mid-latitude region," *Radio Sci.*, vol. 20, no. 3, pp. 643–651, 1985.

[6] V. E. Kunitsyn and E. D. Tereshchenko, *Ionospheric Tomography*. Berlin, Germany: Springer-Verlag, 2003.

[7] Y. A. Liou, A. G. Pavelyev, A. A. Pavelyev, J. Wickert, and T. Schmidt, "Analysis of atmospheric and ionospheric structures using the GPS/MET and CHAMP radio occultation database: A methodological review," *GPS Solutions*, vol. 9, no. 2, pp. 122–143, 2005.

[8] J. K. Lee and F. Kamalabadi, "GPS-based radio tomography with edge-preserving regularization," *IEEE Trans. Geosci. Remote Sens.*, vol. 47, no. 1, pp. 312–324, Jan. 2009, doi:10.1109/TGRS.2008.2001637.

[9] Y. A. Liou, A. G. Pavelyev, S. S. Matyugov, O. I. Yakovlev, and J. Wickert, *Radio Occultation Method for Remote Sensing of the Atmosphere and Ionosphere*, Y. A. Liou, Ed. Vukovar, Croatia: In-The Olajnica, 2010, 170 pp. 45 ill.

[10] Y. A. Liou, A. G. Pavelyev, S.-F. Liu, A. A. Pavelyev, N. Yen, C.-Y. Huang, and C.-J. Fong, "FORMOSAT-3/COSMIC GPS radio occultation mission: Preliminary results," *IEEE Trans. Geosci. Remote Sens.*, vol. 45, no. 11, pp. 3813–3826, Nov. 2007.

[11] Y. A. Liou and A. G. Pavelyev, "Simultaneous observations of radio wave phase and intensity variations for locating the plasma layers in the ionosphere," *Geophys. Res. Lett.*, vol. 33, no. 26, pp. L23 102-1–L23 102-5, 2006.

[12] W. G. Melbourne, *Radio Occultations Using Earth Satellites: A Wave Theory Treatment*, J. H. Yuen, Ed. Pasadena, CA: Deep Space Commun. Navig. Syst. Center Excellence, Jet Propulsion Lab., California Inst. Technol., 2004, ser. Deep space communications and navigation series, JPL California Institute of Technology, Monograph 6, 610 pp.

[13] A. G. Pavelyev, Y.-A. Liou, J. Wickert, T. Schmidt, A. A. Pavelyev, and S. S. Matyugov, "Phase acceleration: A new important parameter in GPS occultation technology," *GPS Solutions*, vol. 14, no. 1, pp. 3–14, 2010. doi:10.1007/s10291-009-0128-1.

[14] A. G. Pavelyev and A. I. Kucherjavenkov, "Refractive attenuation in the planetary atmospheres," *Radio Eng. Electron. Phys.*, vol. 23, no. 10, pp. 13–19, 1978.

[15] A. G. Pavelyev, Y. A. Liou, J. Wickert, A. L. Gavrik, and C. C. Lee, "Eikonal acceleration technique for studying of the Earth and planetary atmospheres by radio occultation method," *Geophys. Res. Lett.*, vol. 36, pp. L21 807-1–L21 807-5, 2009. doi:10.1029/2009GL040979.

[16] S. V. Sokolovskiy, W. Schreiner, C. Rocken, and D. Hunt, "Detection of high-altitude ionospheric irregularities with GPS/MET," *Geophys. Res. Lett.*, vol. 29, no. 3, pp. 621–625, 2002.

[17] V. V. Vorob'ev and T. G. Krasilnikova, "Estimation of accuracy of the atmosphere refractive index recovery from Doppler shift measurements at frequencies used in the NAVSTAR system," *Izv. Russ. Acad. Sci., Phys. Atmosphere Ocean, Engl. Transl.*, vol. 29, no. 10, pp. 602–609, 1994.

[18] D. B. Wen, Y. B. Yuan, J. K. Ou, K. F. Zhang, and K. Liu, "A hybrid reconstruction algorithm for 3-D ionospheric tomography," *IEEE Trans. Geosci. Remote Sens.*, vol. 46, no. 6, pp. 1733–1739, Jun. 2008.

[19] J. Wickert, A. G. Pavelyev, Y. A. Liou, T. Schmidt, C. Reigber, K. Igarashi, A. A. Pavelyev, and S. Matyugov, "Amplitude scintillations in GPS signals as a possible indicator of ionospheric structures," *Geophys. Res. Lett.*, vol. 31, no. 24, pp. L24 801-1–L24 801-4, 2004.

[20] A. G. Pavelyev, Y. A. Liou, and J. Wickert, "Diffractive vector and scalar integrals for bistatic radio holographic remote sensing," *Radio Sci.*, vol. 39, no. 4, pp. RS4 011.1–RS4 011.16, 2004.

[21] K. C. Yeh and C. H. Liu, "Radio wave scintillations in the ionosphere," *Proc. IEEE*, vol. 70, no. 7, pp. 324–360, Apr. 1982.

Alexander G. Pavelyev received the B.Sc. and M.Sc. degrees from Gorky-State University, Gorky, Russia, and the Ph.D. degree in radio physics from the Academy of Sciences of the USSR, Moscow, Russia, in 1969.

He became a Senior Researcher (Assistant Professor) in 1977 and a Leading Researcher in early 1987. He worked as a TAO Fellowship Senior Scientist in the late 1999/early 2000 and as an STA Senior Research Scientist in the late 2000 with CRL, Japan. He was a Visiting Professor with the Radio Science Center for Space and Atmosphere, Kyoto University, Uji, Japan, in early 2001. He worked as a Visiting Professor with the Centre for Space and Remote Sensing Research, National Central University, Jhongli, Taiwan, in 2002, 2003, 2004, 2005, 2006, and 2009. He also worked as a Visiting Professor with the Satellite Positioning for Atmosphere, Climate and Environment Research Centre, Royal Melbourne Institute of Technology University, Melbourne, Australia, in April–May 2010. Since June 2000, he has been the Head of the Laboratory of Radio Wave Propagation in Space, Kotelnikov Institute of Radio Engineering and Electronics, Russian Academy of Sciences, Moscow, Russia.

Kefei Zhang is currently a Professor, the Founder, and the Director of the Satellite Positioning for Atmosphere, Climate and Environment Research Centre, Royal Melbourne Institute of Technology (RMIT) University, Melbourne, Australia. Prior to joining RMIT in the late 1999, he was a Research Fellow with The University of Nottingham, Nottingham, U.K., and was with Wuhan University, Wuhan, China. He is the coinventor of eight international patents, and he has authored over 250 peer-reviewed papers in these fields since 1990 and has attracted more than 12 million dollars in funding from the Australian Research Council, government, and research and industry sectors. He is a regular reviewer of various national and international funding agencies and journals, a member of journal editorial boards, and a frequent speaker/guest at various international events. He is currently the Chief Scientist of the multimillion dollar prestigious Australia Space Research Program Platform Technologies project and leads an international team that comprises a number of international leading scientists in the areas of satellite positioning, space tracking, and atmosphere and climate change research to develop innovation solutions using cutting-edge space technologies. His main areas of expertise are in satellite positioning, navigation, and geodesy. His current research is primarily involved in algorithm development and innovative applications of the GNSS/GPS technologies for high-accuracy positioning, atmospheric studies (e.g. for space weather, space debris surveillance and collision warning, SKA, climate change, weather and environment, and ionosphere), space tracking, satellite orbit determination, and people mobility and object tracking.

Chuan-Sheng Wang received the B.Sc. and M.Sc. degrees from the Department of Civil Engineering, National Chiao Tung University, Hsinchu, Taiwan, in 1998 and 2000, respectively, and the Ph.D. degree in space sciences from the National Central University, Jhongli, Taiwan, in 2009.

He is currently a Research Fellow with the School of Mathematical and Geospatial Sciences, Royal Melbourne Institute of Technology University, Melbourne, Australia. His research interests include precise GPS positioning and GPS meteorology.

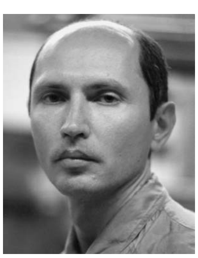

Yuriy Kuleshov received the B.Sc. degree in electronic engineering from the Institute of Radio Engineering, Kharkov, Ukraine, in 1981 and the Ph.D. degree in physics and mathematics from the Institute of Radio Physics and Electronics (IRPE), Academy of Sciences, Kharkov, Ukraine, in 1991.

From 1981 to 1994, he worked with IRPE as a Researcher on the design of the satellite and aircraft microwave remote sensing systems for obtaining environmental information, including the first Soviet space radar of the "Cosmos/Ocean" satellite series, and the aircraft-laboratory multifrequency microwave remote sensing system. He also worked on the development of new methods of deriving, processing, and interpreting environmental information for marine environment (sea ice and iceberg observations, oil spill detection, near-surface wind speed retrieval, and investigations of tropical cyclones) and terrestrial environment (fresh-water ice, glaciers, and vegetation monitoring). Since 1995, he has been the Project Leader at the Australian Bureau of Meteorology (BoM) for the international initiative on "Climate change and tropical cyclones in the Southern Hemisphere: Development of the tropical cyclone archive, climatology and seasonal prediction for the region." He also works on the development of new methods of satellite remote sensing (GPS radio occultation and GPS reflectometry) for applications to climatology and oceanography. He is currently the Australian Team Leader on the Seasonal Climate Prediction Project, Pacific Adaptation Strategy Assistance Program (PASAP) at BoM and an Adjunct Professor with the School of Mathematical and Geospatial Sciences, Royal Melbourne Institute of Technology University, Melbourne, Australia.

Dr. Kuleshov is the Australian representative of the World Meteorological Organization Commission for Climatology Open Panels of Experts on Climate Monitoring and Assessment. He also represents the BoM for the Standards Australia, providing advice and expert opinion on climate science relevant to the committees "Lightning protection" and "Wind actions" activities.

Yuei-An Liou (S'91–M'96–SM'01) received the B.S. degree in electrical engineering (EE) from the National Sun Yat-Sen University, Kaohsiung, Taiwan, in 1987 and the M.S.E. degree in EE, the M.S. degree in atmospheric and space sciences, and the Ph.D. degree in EE and atmospheric, oceanic, and space sciences from the University of Michigan, Ann Arbor, in 1992, 1994, and 1996, respectively.

He is currently a Professor with the Center for Space and Remote Sensing Research, National Central University, Jhongli, Taiwan. He is the author of over 100 refereed papers and more than 200 international conference papers. His current research activities include global positioning system (GPS) meteorology and ionosphere, remote sensing of the atmosphere, land surface, and polar ice, land surface processes modeling, and application of neural networks and fuzzy systems in inversion problems.

Dr. Liou is a member of the Editorial Advisory Board to *GPS Solutions*. He served as the Guest Editor for the June 2005 Special Issue of "GPS Radio Occultation (RO) Experiments," the Associated Editor for the 2008 IEEE *Journal of Selected Topics in Applied Earth Observations and Remote Sensing*, the Editor for the 2009 *Journal of Aeronautics, Astronautics and Aviation*, and the Guest Editor for the January 2010 Special Issue of "Advancements in Atmospheric and Ionospheric Research, Meteorology, Climate Change, Weather Prediction, Oceanography, and Geodesy from GPS Radio Occultation Methods." He serves as the Leading Guest Editor for the IEEE TRANSACTIONS ON GEOSCIENCE AND REMOTE SENSING Special Issue, i.e., "Meteorology, Climate, Ionosphere, Geodesy, and Reflections from the Ocean surfaces: Studies by Radio Occultation Methods." He was a recipient of an Honorary Life Membership with the Korean Society of Remote Sensing in 2007. He was elected as a Foreign Member with the Russian Academy of Engineering Sciences, Moscow, Russia, in 2008. He was the recipient of the Outstanding Alumni Awards from the University of Michigan Alumni Association in Taiwan and the National Sun Yat-Sen University in 2008. He was elected as an Academician by the International Academy of Astronautics in 2009.

Jens Wickert was born in 1963. He received the Ph.D. degree in geophysics/meteorology from Karl-Franzens-University Graz, Graz, Austria, in 2002.

He worked for several years in atmospheric research for the German Weather Service, Alfred-Wegener-Institute for Polar and Marine Research, and German Aerospace Center. Since 1999, he has been with GeoForschungsZentrum Potsdam, Potsdam, Germany, and he is currently the Acting Head of Section 1.1 GPS/Galileo Earth Observation. He is responsible for various GNSS-related research projects. He is the author and coauthor of numerous papers related to GNSS remote sensing in peer-reviewed journals.